A B-Scan Imaging Method of Conductivity Variation Detection for Magneto–Acousto–Electrical Tomography

MING DAI[1], **(Member, IEEE), TONG SUN**[1], **XIN CHEN**[1], **LINGYAO YU**[2,3], **MIAN CHEN**[1], **PENGHUI HAO**[1], **XIN ZENG**[1], **JIEJIE YAN**[1], **AND SIPING CHEN**[1]

[1]National-Regional Key Technology Engineering Laboratory for Medical Ultrasound, Guangdong Key Laboratory for Biomedical Measurements and Ultrasound Imaging, Health Science Center, School of Biomedical Engineering, Shenzhen University, Shenzhen 518055, China
[2]Guangxi Key Laboratory of Automatic Detecting Technology and Instruments, Guilin University of Electronic Technology, Guilin 541004, China
[3]Guangxi Key Laboratory of Optoelectronic Information Processing, Guilin University of Electronic Technology, Guilin 541004, China

Corresponding authors: Xin Chen (chenxin@szu.edu.cn) and Siping Chen (chensiping@szu.edu.cn)

ABSTRACT Based on the Hall effect, a magneto-acousto-electrical tomography (MAET) has been indicated to have a good ability for distinguishing the conductivity variations along the acoustic propagation direction, and B-scan imaging of the MAET is expected to obtain pathological information of the tissue. For achieving a clear B-scan image, in this paper, we designed and implemented a MAET system with a planar transducer and conducted a series of experiments to explore the characteristics of the magneto-acoustic-electrical (MAE) signal and electromagnetic interference (EMI) signal. The influence of the EMI signal on the MAE voltage signal was demonstrated experimentally, and the generation mechanism of the EMI signal was explained. Concurrently, several effective methods were proposed for reducing the EMI signal and improving the imaging resolution of the B-scan image. Additionally, for obtaining a B-scan image with high resolution, the detection front end was redesigned and algorithms applying the characteristics of the MAE signal were proposed. The accuracy, feasibility, and effectiveness of the improved methods were verified. Finally, a B-scan image was reconstructed with the relative amplitude of the conductivity. The results showed that: 1) the MAE signal obtained by the redesigned platform could be well separated from the EMI signal and had a higher SNR than that obtained by the previous detection system; 2) the proposed imaging algorithms had a high detection accuracy and achieved an axis resolution of 1 mm on the z-axis; and 3) the interfaces of the conductivity changes of homogeneous phantoms with 0.5% salinity were clearly presented by measuring the MAE wave packets, and the measured thicknesses of the phantoms were highly consistent with the actual thicknesses. This paper provides a theoretical and experimental basis for detecting the interface positions of conductivity variation, and the presented MAET technology is expected to become an alternative medical imaging modality for the early diagnosis and detection of biological cancerous tissues.

INDEX TERMS Conductivity distribution, Hilbert transform, electromagnetic interference, weak signal processing and detection, magneto–acousto–electrical voltage.

I. INTRODUCTION

Previous researches have illustrated that the variation in conductivity within a tissue is associated with cancer. For example, the conductivity variation in a normal tissue differs from that in a tumor liver tissue by more than 50% [1], and the conductivity value of muscle is close to 10 times that of fat [2]. Thus, the apparent conductivity difference can be

The associate editor coordinating the review of this manuscript and approving it for publication was Zehong Cao.

exploited as a sensitive indicator for pathological detection. Because a variation in conductivity is a typical characteristic of most tumors in their early stage [3] and the early diagnosis of tumor can significantly reduce the cancer mortality [4], [5]. Therefore, conductivity imaging is expected to become one of the most effective tumor assessment technologies in the future [1].

Until now, several approaches have been developed for imaging conductivity including electrical impedance tomography (EIT) [6], [7], magnetic resonance electrical impedance

tomography (MREIT) [8], magneto–acoustic tomography, and magnetic induction tomography (MIT). Among the above-mentioned imaging modalities, imaging conductivity in the conductive sample could be achieved by EIT [9], [10]. However, EIT has a low spatial resolution because of the ill-posed nature of the inverse problem [11]. Concurrently, it is still severely restricted by the quantity of the electrodes, electrical insulation of the target sample, and high-current injection. Its practical performance is also limited by the low spatial resolution and reconstruction algorithms [12]. Furthermore, in the methods of EIT, acousto–electric imaging, and MREIT [13], electrical currents are injected in the target sample by one or more pairs of surface electrodes [14]. Owing to a low-conductivity layer surrounding the target sample, the shield effect occurs, making it difficult to image the conductivity of deep biological samples with a high spatial resolution using EIT. MIT stimulates a biological sample with a time-variant magnetic field and measures the weak secondary magnetic field to reconstruct the conductivity [15]. Nevertheless, capacitive coupling between an excitation coil and a receiving coil contaminates the measured value at the receiver, the secondary signal gradually weakens and easily superimposed by the primary signal from the transmitter, and a high-strength transient stimulation magnetic field is needed. Therefore, several other types of imaging modalities, such as magneto–acoustic tomography and magneto–acoustic–electrical tomography (MAET), also called the Lorentz force electrical impedance tomography (LFEIT) [16], [17], have been developed to improve the spatial resolution and contrast. Because MAET [18]–[20] combines the advantages of the acoustic, electric, and magnetic fields and those of both the ultrasonography and traditional EIT [21], and the magneto–acoustic–electrical (MAE) voltage detected by a pair of electrodes is measured and processed flexibly [22], [23]. Thus, MAET is extensively investigated worldwide and may achieve widespread applications [18], [19]. It has also generated a strong interest among many researchers in the field of the conductivity imaging. For example, Wen et al. originally proposed the Hall effect imaging [24], a method subsequently named MAET [19], and this theoretical basis laid the foundation for the research on MAET [25]. Roth and Schalte [26] presented a series of methods for MAET and clarified several limitations of the methods. In addition, the forward and inverse problems [27] were intensively studied by Xu and He [28], and they derived MAE voltage signals of a slab using electrodes and imaged the conductivity via an ultrasound scan on a plane. Li *et al.* [19] employed a high-voltage stimulation signal with a narrow pulse to activate an ultrasound transducer and imaged a low-conductivity animal gelatin phantom by a pair of electrodes, illustrated that the conductivity variation interface could be measured accurately. Yu *et al.* [29] designed an experimental set-up of the MAET measurement with a sinusoid-Barker-coded excitation and obtained clear MAE signals of a three-layered

gel phantom. In [22] and [30], the low-instantaneous peak power of an ultrasonic transducer was used by combining the coherent frequency demodulation method and a linear frequency modulated ultrasound pulse. In [31], a bovine muscle sample was imaged using the measured voltage with LFEIT. In [18], both a single and multi-focus MAET system with a chirp pulse stimulation were introduced for B-scan image. The effect of the stimulation position on the amplitudes of the conductivity variation was clearly demonstrated. In [32], the MAE voltage was illustrated to have the capability of differentiating the conductivity changes along the direction of the ultrasonic propagation.

Although the tremendous progress has been made in the interface detection of the conductivity variation and the clear MAE signals were obtained by Li *et al.* [19], Wen *et al.* [24], and Yan *et al.* [32], respectively, it seems that they have not yet described the existence of the electromagnetic interference (EMI) signal and its influence on the MAE signal. In fact, the MAE signal is doped with the EMI signal, which affects the imaging effect of the B-scan image. In [33], The EMI signal generated by the instantaneous excitation of the probe can be obviously seen near the original position. In [23], conspicuous EMI signal generated by the probe's instantaneous excitation can also be detected, which demonstrates that the influence of the probe excitation on the detection signal, and also shows the existence of the EMI signal. As the EMI signals caused by the reflection of the interfaces and the container bottom are much weaker than the EMI signal generated by the probe's instantaneous excitation, the former EMI signals are often ignored. Thus, investigation on a low-complexity, non-intrusive, low-cost MAET detection system that can well eliminate the EMI signal and detect the interface positions of the conductivity variation is highly significant. To explore the methods for separating the MAE signal from the EMI signal and achieve a clear B-scan image with conductivity information, in this work, we derived the formulas for conductivity imaging with one-dimensional (1D) MAET and designed a B-scan MAE imaging platform. We also experimentally demonstrated the influence of the EMI signal on the MAE voltage and proposed several effective methods for reducing the EMI signals and improving the signal-to-noise ratio (SNR) of the system. In addition, we redesigned the experimental platform, clearly obtained the MAE wave packets after several improvements, and found that the positions of the conductivity variation interfaces were consistent with the actual measured positions. Moreover, in this study, a B-mode imaging algorithm was proposed, and a clear B-scan image using the relative amplitude of the conductivity was obtained. The measured conductivity boundary showed good agreement with the thickness of the target sample, which proved the accuracy and feasibility of the proposed B-scan algorithm. The presented approaches provide the possibility of the boundary detection of tumors in the future.

II. IMAGING PRINCIPLE AND METHOD

A. IMAGING PRINCIPLE

Based on the coupling of the acoustic, electric, and magnetic fields, MAET is expected to become a non-invasive detection method for biological tissues. In MAET, using a permanent magnetic field a beam of ultrasound pulse excitation is applied to a target imaging sample to excite its local particles to vibrate with the propagation of the acoustic wave. The positively and negatively charged local particles are separated owing to the opposing Lorentz forces generated by the ultrasonic wave and static magnetic field. Subsequently, electrical current field distribution occurs in the target sample, and a MAE voltage on the surface of the target sample is detected. As a nonzero MAE voltage only arises from the positions where a gradient of conductivity exists [24], i.e., when the wave packet passes a conductivity variation interface, the total MAE current signal becomes nonzero and the resulting MAE voltage indicates the presence of the corresponding interface [24]. Therefore, after scanning around a target sample using an ultrasound stimulation transducer, a B-scan image of the imaging body can be derived using the corresponding reconstructed algorithms. A schematic of the MAET detection system is shown in Fig. 1.
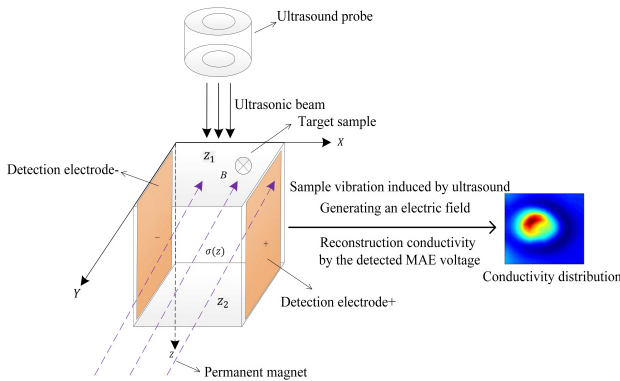

FIGURE 1. Schematic of MAET detection system.

In our study, a sinusoidal excitation signal was applied to an ultrasound planar probe to generate vibration for interacting with a uniform static field, B, to produce the Lorentz force. Therefore, a local electric current was generated, and the MAE voltage signal was detected by a pair of electrodes placed on both sides of the target phantom. According to the MAET detection theory, several MAE voltage peaks with the interface information of the conductivity variations can be obtained by moving the probe and repeating the detection operations. A B-scan image in a plane can be obtained after combining the collected MAE voltage signals with the scanning information of the probe.

To simplify the principle derivation, assumptions are made for acoustic propagation in an ideal fluid without energy loss and viscosity, and the acoustic pressure is low without the consideration of the nonlinear effect. Therefore, the acoustic pressure satisfies the wave equation [27], and denoting the

ultrasound pressure wave as $p(z, t)$, the vibration velocity at (z, t) can be written as [27]

$$v(z, t) = -\frac{1}{\rho(z)} \int_0^t \frac{\partial p(z, t)}{\partial z} dt \qquad (1)$$

Under the stimulation of an ultrasonic beam, the vibration of a charged ion, q, occurs with a certain velocity. Owing to the interaction with the static magnetic field, ion deflection occurs, generating the Lorentz force, which is perpendicular to the vibration velocity and magnetic field. The Lorentz force can be calculated as

$$F = qv \times B \qquad (2)$$

where v is the vibration velocity of the particle, B is the static magnetic field, and F is the Lorentz force.

A single charge, q, experiences an electric field source, $E = v \times B$. This generates the Lorentz force, which in turn establishes a current density, J, in the target tissue. The current density can be expressed as

$$J = \sigma v \times B \qquad (3)$$

Integrating J over the ultrasound beam width, W, and ultrasound path, the net current can be obtained in the form of Eq. (4).

$$I(t) = WB \int_{soundpath} \sigma(z) v(z, t) dz \qquad (4)$$

In practice, the detected voltage measured by a pair of electrodes is only a part of the voltage caused by the Lorentz force. Therefore, the received amplitude of the voltage can be denoted as

$$V(t) = kWR_s B \int_{soundpath} \sigma(z) v(z, t) dz \qquad (5)$$

where k is the fraction of the total voltage induced by the Lorentz force and R_s is the impedance of the detection circuit.

By substituting the particle vibration velocity in Eq. (5), the detected MAE signal can be expressed as follows:

$$V(t) = -kWR_s B \int_{soundpath} \frac{\sigma(z)}{\rho(z)} \left[\int_0^t \frac{\partial p(z, t)}{\partial z} dt \right] dz \qquad (6)$$

Integrating Eq. (6) by parts and assuming the excitation ultrasonic wave propagates from position z1 to z2, we derive Eq. (7).

$$V(t) = -\frac{kWR_s B \sigma(z)}{\rho(z)} \int_{-\infty}^t p(z, t) dt |_{z1}^{z2}$$
$$+ kWR_s B \int_{z1}^{z2} \left(\frac{\partial}{\partial z} \left(\frac{\sigma(z)}{\rho(z)} \right) \int_{-\infty}^t p(z, t) dt \right) dz \qquad (7)$$

Assuming $M(z, t) = \int_{-\infty}^t p(z, t) dt$, Eq. (7) can be rewritten as

$$V(t) = \frac{kWR_s B}{\rho(z)} \int_{z1}^{z2} \left(\frac{\partial \sigma(z)}{\partial z} \right) M(z, t)) dz - \frac{kWR_s B \sigma(z)}{\rho(z)} M(z, t)|_{z1}^{z2} \qquad (8)$$

Because the excitation ultrasonic beam propagates from position $z1$ to $z2$, the integral of the ultrasonic burst is equal to 0 at any time of the interval enclosing the entire burst, i.e., $M(z, t) = 0$. Thus, the second term of the right-hand side of Eq. (8) is 0. Assuming that the mass density of the target tissue is uniform, i.e., ρ_0, Eq. (8) can be simplified as:

$$V(t) = \frac{kWR_sB}{\rho_0} \int_{z1}^{z2} (\frac{\partial\sigma(z)}{\partial z}M(z, t))dz \qquad (9)$$

B. IMAGING METHOD

The momentum of an ultrasonic beam is carried by the wave packet when it travels along the direction of the ultrasonic propagation. As the packet passes through the conductivity variation interfaces successively, the integrand in Eq. (9) becomes nonzero, generating a weak Hall voltage. The peak of the detected Hall voltage represents the positions of the conductivity variation interfaces of the phantom. Thus, the time of each peak indicates the position of its corresponding interface, i.e., converting spatial information to time-dependent information. In addition, the imaging process is similar to that of the traditional echo ultrasound imaging. Therefore, a B-scan image or multidimensional scan image can be obtained using the conductivity information after combining many 1D MAE voltage signals at different excitation positions with their corresponding location information.

III. SYSTEM DESIGN
A. PLATFORM DESIGN

To investigate the generation mechanism of the EMI signals, effect of the EMI signals on the MAE signals, and methods to reduce the EMI signals and obtain a clear B-scan image in this work, we designed an MAET detection system. The system included three parts: 1) excitation section, 2) probe motion control platform, and 3) acquisition and processing platform. As the major part of the system, the platform for the acquisition and processing was composed of an acquisition front end, two amplifiers, a band-pass filter, and a digital oscilloscope. The acquisition front end included a C-shaped permanent magnet with two cube magnets and its support structure, plastic detection sink inserted into the C-shaped static magnet, and pair of silver-plated copper electrodes of size $53 \times 31.5 \times 1$ mm. A connection schematic of the MAET detection system is shown in Fig. 2.

In our MAET apparatus, the high-power immersion-type probe (custom-made, Blatek Inc., USA) is utilized as an excitation transducer, and the motion platform (MC600, ZOLIX Instruments Inc., Beijing, China) is utilized for movement. The target uniform phantom is fixed in a plastic detection sink container and placed in the center of the C-shaped static magnetic field ($100 \times 90 \times 40$ mm) at an intensity of approximately 0.45 T, which is produced by two cube Nd–Fe–B magnets (100 mm × 100 mm × 40 mm). To receive a stable voltage signal and minimize the electrode–phantom contact impedance, the pressure between the electrode and phantom is ensured to be constant. In addition, two detection electrodes
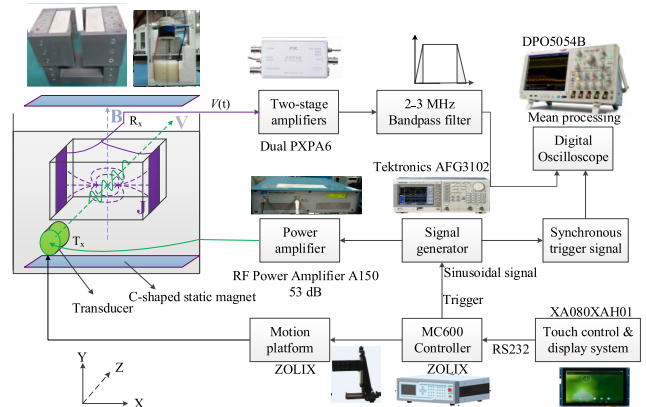

FIGURE 2. Connection schematic of proposed MAET system.

having the same shape and size are manufactured and placed closely to both sides of the target sample.

During the data collection and processing with the proposed MAET detection system, first, the touch-control display system sends the motion control command to the MC600 controller through an RS-232 serial port. The motion controller moves the excitation probe to the target position and generates a trigger signal to switch the signal generator on or off. At each trigger, an excitation signal with two cycles of sinusoidal pulses, a center frequency of 2.5 MHz, an amplitude of 600 mV, and repetition time of 10 ms is produced by the signal generator (AFG3102, Tektronics Inc., USA). Then the excitation signal is sent to the high-power probe after a 53-dB power amplification (RF Power Amplifier A150, Electronics & innovation Inc., New York, USA). Subsequently, a synchronous trigger signal is generated by the signal generator and sent to the digital oscilloscope, and local particle vibrations are generated in the target sample under the excitation of the ultrasonic probe. The vibrating particles placed under the action of a static magnetic field generate the Lorentz force, which produces weak MAE voltage signals perpendicular to the direction of the electric and magnetic fields. Concurrently, two silver-plated copper electrodes are tightly attached to both sides of the target phantom and connected to the differential multi-stage amplifier (PXPA6, Pengxiang technology Inc., Changsha, China) after a 50-Ω input impedance. The MAE voltage signals are sent to a 2–3 MHz band-pass filter after an 80-dB amplification achieved by two differential multi-stage amplifiers. Subsequently, the MAE signal along the z-axis is received by the digital multi-channel oscilloscope (DPO5054B, Tektronics Inc., USA) at a sampling frequency of 20 MHz. After mean processing of the MAE voltage more than 3000 times, the digital oscilloscope displays and stores the MAE voltage as comma separated value (CSV-formatted data). Finally, the stored CSV data is processed offline in MATLAB 2015a environment, and the MAE voltage along the ultrasonic propagation direction is derived. By moving the transducer to the next position and repeating the above

operation, the corresponding MAE voltage signals at different scanning positions are obtained for imaging the positions of the conductivity variations. A B-scan image using the relative amplitude of the conductivity is obtained after the imaging algorithms combine the MAE voltages along the *z*-axis with the corresponding position information on the *x*-axis.

B. IMAGING ALGORITHMS

Based on the detection platform, the offline data was averaged 3500 times for a high imaging resolution. The conventional Wiener filtering in the time domain was performed for the averaged data. Then, the envelope distribution of the MAE voltage was obtained by a Hilbert transform. Next, a reconstructed B-mode image of the MAE voltage distribution was derived after combining the MAE voltage signals at the different excitation positions. Finally, a B-scan image using the relative amplitude of the conductivity was obtained after performing a linear interpolation algorithm. In the B-mode imaging process, Wiener filtering was used to filter out the external noise and reduce its interference in the MAE signal. Hilbert transform was used to obtain the envelope of the MAE signal and convert the MAE wave packet with polarity changes of "$+/-$" into a unipolar wave packet for achieving high-accuracy interface position detection of the conductivity variations.

IV. EXPERIMENTS AND RESULTS

A. PERFORMANCE EXPERIMENTS

To investigate the characteristics of the MAE signal and EMI signal, generation mechanism of the latter, and influence of the EMI signal on the MAE voltage signal, sodium chloride (NaCl), pig-skin powder, and water were chosen to form a homogeneous phantom with conductivity similar to that of a biological tissue. Moreover, a uniform phantom of 0.5% salinity (7.5 × 3.0 × 3.5 cm) was fixed to the bottom of a plastic shell and used as the target sample to conduct the performance tests. Both the electrodes and phantom were placed in the static magnetic field, and the phantom was fixed at approximately 4.5 cm in front of the stimulating probe. As shown in Fig. 3 (a), the distance from a (probe) to b (first interface) is 4.44 cm and from a to c (second interface) is 7.44 cm. After the ultrasonic beam is reflected by the bottom of the plastic shell, the total sound path from a to c and then to b is 10.44 cm. Concurrently, the ultrasonic beam is reflected at the upper and lower interfaces of the phantom and container bottom. Then, the reflected ultrasound echoes are received by the probe, and the relative positions in this process are shown in Fig. 3 (b). The total sound path from a to b/c and then back to a is 8.88/14.88 cm.

As the target sample was placed in deionized water, the propagation speed of the ultrasound was calculated at 1490 m/s. The voltage signals received by the detection electrodes after scale conversion are shown in Figure 4. Three MAE wave packets appear at approximately 4.464, 7.43, and 10.53 cm. The corresponding amplitudes are 10.02, −7.729,
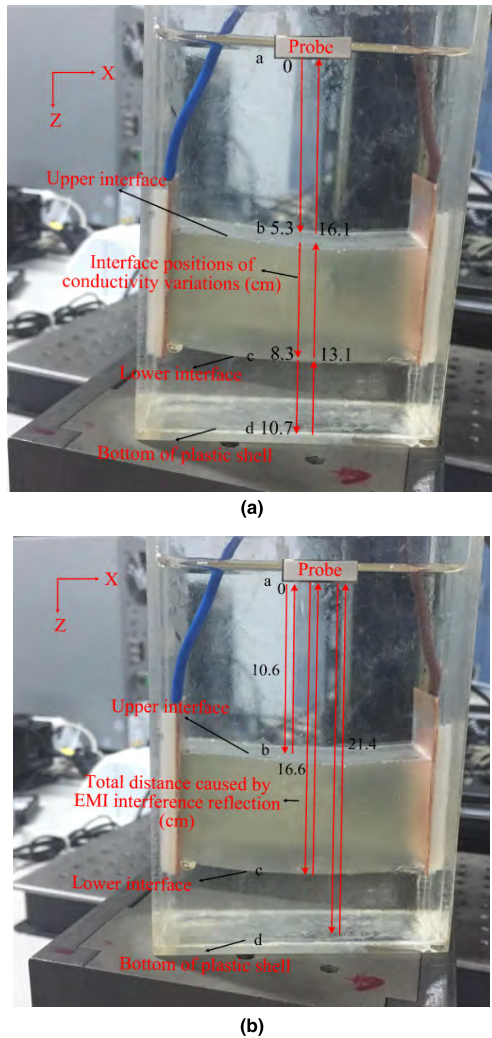

(a)

(b)
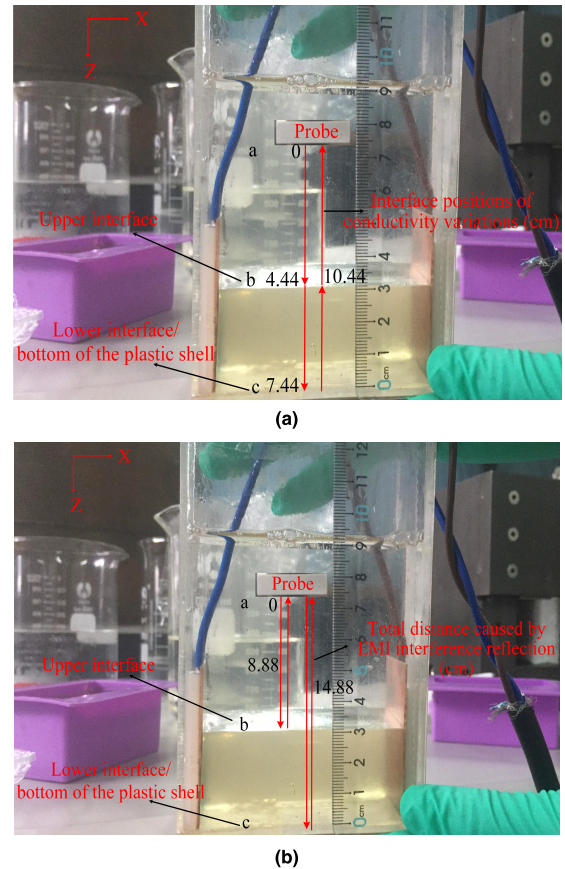
FIGURE 3. Relative interface positions. (a) Three interface positions of conductivity variation. (b) Reflection positions of two interfaces.
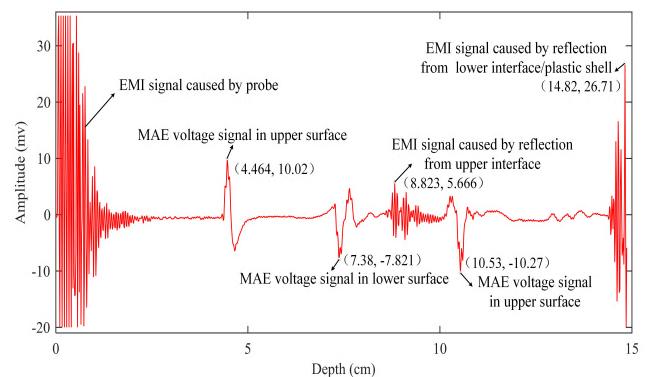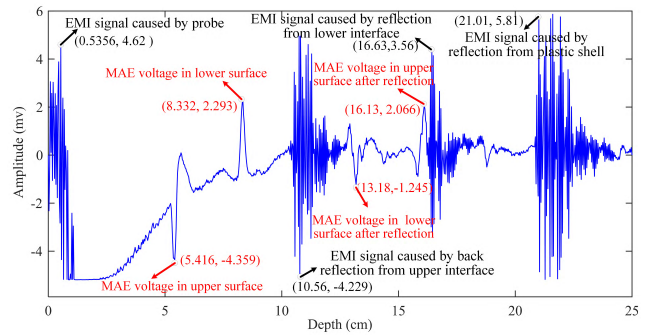

FIGURE 4. Three MAE voltage signals and EMI signals.

and −10.27 mV, respectively. Therefore, the measured distance between the upper interface and lower interface is 2.916 cm, and the distance from the bottom reflection interface to the upper interface is 3.15 cm. Thus, the calculated mean value of the thickness of the phantom is 3.033 cm, which is consistent with the actual thickness. The above three interface positions of the MAE signal show good agreement with the three interface positions of the conductivity variation. Moreover, the position of the EMI wave packet caused by the reflection of the upper and lower interface of the phantom is 8.823 cm and 14.82 cm, respectively, the amplitude of

(a)

(b)

FIGURE 5. Relative interface positions of the phantom. (a) Four interface positions of conductivity variation. (b) Measured reflection positions.

the two EMI signals is 5.666 mV and 26.71 mV, respectively. The reflection positions of the EMI signals measured by our detection system are highly consistent with those of the actual reflection interfaces of the two interfaces, which prove that our MAET system could be used to measure the interface positions by detecting the EMI signals.

To further test the performance of our proposed MAET detection system and explore the generation mechanism and characteristics of the EMI signal, the target phantom was pulled up approximately 2.4 cm and the same experiments were performed under the same experimental conditions. The relative positions of the uniform phantom are shown in Fig. 5. The distance from a to b is 5.3 cm, from a to c is 8.3 cm, and from a to d (bottom of the plastic shell) is 10.7 cm. After the ultrasonic beam is reflected by the bottom of the plastic shell, the ultrasonic beam arrives at c and then goes to b. The total sound path from a to d and then to c/b is 13.1 cm/16.1 cm. In addition, the total sound path after the ultrasonic reflection at the upper interface, lower

FIGURE 6. Four MAE voltage signals and EMI signals.

interface, and container bottom is approximately 10.6 cm, 16.6 cm, and 21.14 cm, respectively. The three total sound paths and relative positions of the phantom are shown in Fig. 5(b).

Based on the same principle, after scale conversion, similar results were obtained, as shown in Fig. 6. Four MAE narrow wave packets are clearly seen with opposite changes in polarity, and they appear at approximately 5.416, 8.332, 13.18, and 16.13 cm. They indicate the conductivity variations at the corresponding interfaces, where the first and third MAE wave packets and the second and fourth MAE wave packets having the same polarity changes of "+/−" are observed. Moreover, wave packets of the MAE voltage are derived at the phantom interfaces with the amplitudes and vibration polarities representing the values and directions of the conductivity variations. Additionally, the positions of the EMI wave packets caused by the reflection of the upper interfaces, lower interfaces, and container bottom appear at approximately 10.56, 16.63, and 21.01 cm, and their relative amplitudes vary from 4.299 to 3.56 to 5.81 mV. The measured positions of the three EMI wave packets are highly consistent with the actual reflection positions of the three interfaces, and the thickness of the phantom obtained by calculating the interface positions of the EMI wave packets agrees with its actual thickness.

Additionally, a second experiment provided more information of the MAE wave packets and further demonstrated the correctness, feasibility, and accuracy of our detection system. Both the characteristics of the MAE wave packets and EMI wave packets are clearly presented in Fig. 4 and 6, and the interface positions of the conductivity variations measured by our proposed system are highly consistent with the mean values obtained by the ultrasound B-mode (the actual values). Moreover, the thickness of the phantom, obtained by detecting the EMI wave packets or the MAE wave packets, is consistent with its actual thickness, which indicates that the interface positions of the conductivity variations can be determined by detecting the MAE wave packets. The accuracy of the system is found to be high, and the thickness and interface positions of the phantom can be measured by our proposed MAET detection system using the detection of both the EMI wave packets and MAE wave packets.

In the above-mentioned two experiments, when the ultrasonic probe excited the phantom, a single element of the probe generated a vibration after it was stimulated instantly by hundreds of volts. Consequently, an EMI signal was instantly generated under the action of the inverse piezoelectric effect. Next, the ultrasound beam passed through the phantom, and according to Eq. (9), generation of MAE signals occurred at the positions of the gradient of conductivity. Therefore, MAE wave packets were generated at both the upper interface and lower interface of the target phantom. Subsequently, the ultrasound beam passed through the phantom again after the bottom reflection, and two MAE wave packets were also generated at two interface positions. Concurrently, a part of the ultrasonic beam was reflected at the upper interface of the phantom, and the reflected ultrasonic echo was received by the probe. Then, an EMI signal was generated under the action of the piezoelectric effect. Because the two detecting electrodes were equivalent to a pair of antennas, the EMI signal was also collected by them. Similarly, when the ultrasonic beam reached the lower interface and container bottom, ultrasonic reflection occurred at both the lower interface and container bottom. Then, two ultrasonic echoes were received by the probe and single-element of the probe, generating vibration, which could be regarded as the signal source. Thus, the piezoelectric wafer of the probe emitted two EMI signals under the piezoelectric effect. Finally, the EMI signals were transmitted to the detecting electrode in the form of an electromagnetic wave.

As the EMI signals were generated by the vibration of the array element of the probe, the propagation speed of the electromagnetic wave was 3.0×10^8 m/s, which was higher than the ultrasound velocity. Moreover, the distance from the probe to the electrode was short, and so, the propagation delay of the EMI signal was negligible in the process of detecting the EMI wave packet. Thus, the EMI signal can only be used to detect the container bottom and boundary of the phantom, and it is impossible to measure a region having a variation in conductivity but no internal interface. Therefore, in this paper, methods of detecting the MAE wave packets for imaging a B-scan image are proposed.

B. IMPROVEMENTS OF SYSTEM ACQUISITION PLATFORM

Under the inverse piezoelectric effect, the first EMI signal caused by the probe was obtained after it was stimulated instantly by hundreds of volts, and the amplitude of the EMI signal detected by electrodes could reach at the millivolt level without amplification. Thus, the EMI signals needed to be shielded and filtered. Because both the MAE signals and EMI signals were mixed together, it was necessary to eliminate the EMI signals from the detected voltage. Thus, a method to separate the MAE signal from the EMI signal and improve the system SNR was urgently needed.

Because the EMI signal is caused by the ultrasonic echo back-reflected from the interface, the sound path is twice that of the MAE signal at the interface. Therefore, the MAE signal can be separated from the EMI signal, and the EMI

signal can be significantly reduced by extending the distance from the probe to the target sample. The EMI signal becomes increasingly weaker as the distance increases. In our work, a simulation of the excitation probe was performed by the modeling software, COMSOL Multiphysics [34], according to the parameter characteristics of the probe. The simulation results showed that the amplitude of the ultrasonic pressure of the probe at the position of 167.785 mm was maximum. This demonstrated that the excitation of the far field of the probe can not only reduce the EMI signal, but also make the amplitude of the received MAE signal large. In addition, the MAE and EMI signals can be separated using the above described method. Concurrently, the electromagnetic radiation interference was gradually reduced as the excitation depth increased. Moreover, several methods for improving the detection front end are proposed in this paper, such as increasing the magnet space from $10 \times 10 \times 4$ cm to $24 \times 24 \times 6$ cm and increasing the field strength of the static magnet from 0.45 to 0.78 T. As the NaCl within the phantom was evenly distributed, the salinity inside the phantom was easy to dilute in deionized water. Therefore, to improve the system SNR, enhance the measurement accuracy of the MAE signals, and reduce the EMI signals, in the following experiments, an electromagnetic shielding silicone box was employed. To overcome the external noise interference, double-shielded cables were utilized. The outermost layers of the shielded wire were connected to the ground at a single point. The wires connecting to the electrodes were wrapped with metal copper foil, which was connected to the ground. In addition, the acoustic coupling medium was changed from deionized water to insulating oil for a better magnetic shielding effect.

Furthermore, to avoid the EMI signal caused by the ultrasonic back-and-forth reflection between the probe and bottom interface, an ultrasound-absorbing material was placed at the bottom of the container. To reduce the influence of the EMI signal or external noise on the MAE voltage, a double-shielded transmission cable and shielding network were used to improve the system SNR. Given the non-uniformity of the magnetic field between the two magnets, the target sample was placed in their middle to the maximum extent. To facilitate the free movement of the transducer, eliminate the EMI signal, and decrease the impact of intermittent air on the imaging body. Insulating oil was used as the coupling agent between the stimulating probe and target sample in our experiment.

Moreover, the plastic shell and support structure of the probe were redesigned and fabricated, and an electromagnetic shielding box was manufactured with a sound-permeable silicone material and placed in the plastic shell. The electrodes and target phantom were placed in the electromagnetic shielding box. During the ultrasonic excitation process, insulating oil was poured into the silicone box and plastic shell for good acoustic coupling. The probe emitted ultrasonic waves, which passed through the silicone shielding box and stimulated the phantom. The above methods significantly reduced the propagation of the EMI signal between the probe and electrodes,
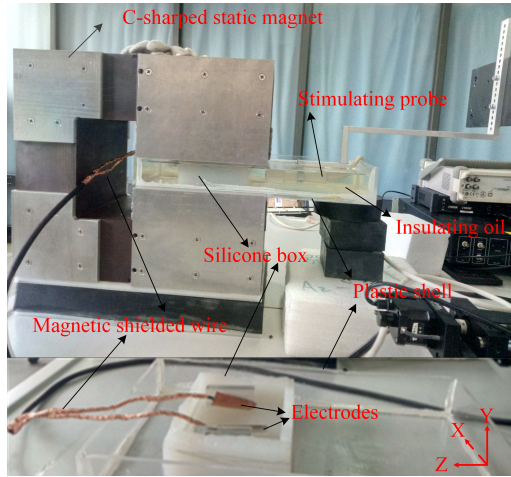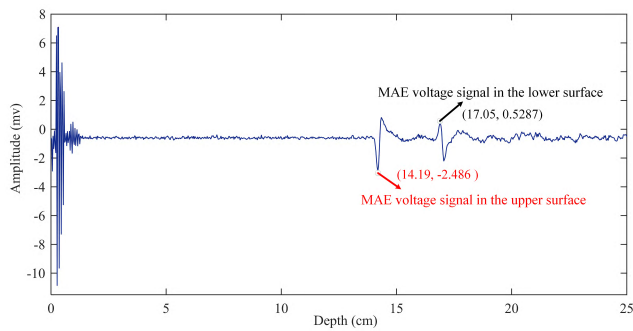
FIGURE 7. System detection front end.

FIGURE 8. MAE voltage signals after several improvements.

thereby strongly reducing the EMI signal and increasing the SNR. The redesigned detection front end of this system is presented in Fig. 7.

C. SYSTEM PERFORMANCE TEST AFTER IMPROVEMENTS
To investigate the effects of the newly designed acquisition front end and test the feasibility of the improved MAET detection system, a homogeneous imitation ($75 \times 28 \times 30$ mm) with 0.5% salinity and 2.80 cm thickness was utilized as the imaging sample to perform the conductivity performance tests. The redesigned MAET detection front end is shown in Fig. 7. A single-element ultrasonic stimulating transducer was placed on the right side of the phantom, it was used to vertically excited the upper surface of the phantom. The movement of the excitation probe was driven by the motion controller for scanning around the surface of the target sample in a straight line. Data acquisitions from the electrodes were averaged, displayed, and stored in a multichannel oscilloscope. As shown in Fig. 8, we obtain an MAE signal with a high SNR in which two MAE narrow wave packets are displayed clearly with opposite vibration polarities, representing the conductivity variations at the corresponding interfaces. The positions of the upper and lower interfaces of the imitation are 14.19 cm and 17.05 cm, respectively and the

corresponding amplitudes are -2.464 and 0.5287 mV. Thus, the measured thickness of the phantom by calculating the distance of the two interfaces is 2.86 cm.

Additionally, the ultrasound B-mode imaging technology was utilized to measure the average thickness of the target phantom. Three position points of each interface of the B-mode imaging were randomly extracted and averaged. The average distance of the two interfaces of the conductivity variation was appropriately 2.80 cm and employed as the actual value.
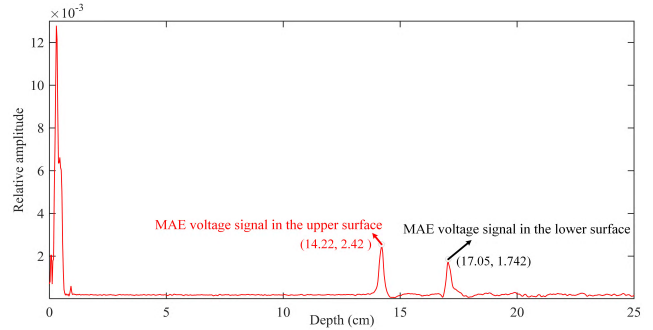

FIGURE 9. MAE voltage signals after imaging algorithms.

Moreover, to further improve the accuracy of the conductivity detection, conventional Wiener filtering was utilized to reduce the interference of the external noise in the MAE signal. The Hilbert transform was employed to derive the envelope of the MAE signal. The mean calculation was performed thousands of times to filter out the external noise. High-SNR received MAE wave packets were clearly observed after processing by the above algorithms, and as shown in Fig. 9, the upper and lower interfaces of the phantom are easily distinguished, with the two peaks at the interfaces appearing at approximately 14.22 and 17.05 cm, respectively. Thus, the thickness of the phantom is approximately 2.83 cm, which shows good agreement with the actual thickness and measured thickness.

In addition, B-scan motion was performed, and the step-scan movement on the *x*-axis was set as 1 mm. The stepping motion along the *x*-axis was performed 20 times, and therefore, 20 MAE signals were derived. The average distance of the two interfaces was obtained by measuring the two peak points of each MAE voltage, and the result illustrated that the mean value achieved by our redesigned MAET detection system was close to the mean value obtained by the ultrasound B-mode.

After the mean calculation, Wiener filtering, and Hilbert transform, B-scan imaging and a linear interpolation algorithm were applied to the MAE voltage signals at different excitation positions. The reconstructed B-scan image was derived by moving the probe and scanning the uniform phantom along the *x*-axis direction. As shown in Fig. 10, the upper and lower interfaces of the imitation can be clearly distinguished, and the average positions of the conductivity variations of the upper and lower interfaces of the phantom
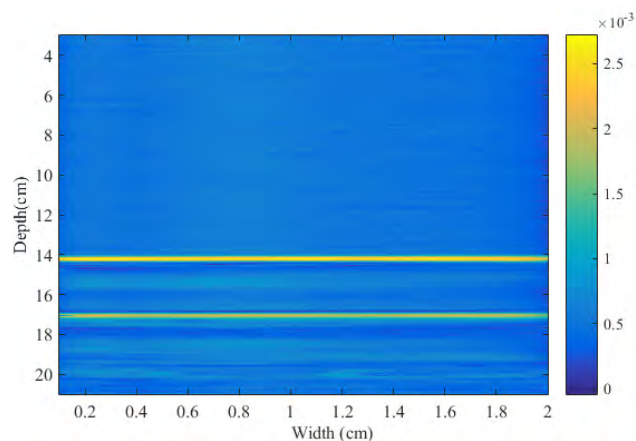
FIGURE 10. Reconstructed B-scan image of homogeneous phantom with 0.5% salinity.

are approximately 14.21 and 17.03 cm, respectively. The average thickness of the target phantom is approximately 2.82 cm, which demonstrates that the interface positions of the conductivity variation and thickness of the phantom measured by our redesigned system exhibit good agreement with the corresponding actual values. These results validate the accuracy of our proposed MAET detection system on the *z*-axis, reveal the feasibility of the imaging method and indicate that the proposed system and imaging algorithms can be applied to detect the interfaces of the conductivity variations of phantoms. Moreover, the results show that the interface positions can be detected by measuring the EMI signals.

V. DISCUSSION

MAET is a novel developing method that combines the good contrast of conductivity imaging with the high-spatial resolution of sonography. Based on the theory of Hall effect imaging, a MAET system by imaging the electrical conductivity with a noninvasive measurement was implemented, and the equations satisfying a 1D MAET detection system were given. The feasibility and performances of the detection system were assessed experimentally by two similar experiments and a B-scan experiment. As shown in Figs. 4 and 6, the μv-level MAE signal is very weak and sensitively affected by the external noise. Moreover, the EMI signal caused by the interface reflection is weaker than the mv-level EMI signal generated by the instantaneous excitation of the probe. Compared with the MAE voltage, the EMI signals have larger amplitudes. Therefore, a low-noise high-sensitive MAET system with a new detection front end and B-scan imaging algorithm was redesigned to obtain clear MAE signals and minimize the EMI signals. Compared with the old detection system, the newly designed platform could significantly reduce the EMI signal, improve the SNR of the MAE signal, and well separate the MAE signal from the EMI signal, which are shown in Figs. 4, 6, and 8.

Moreover, as shown in Figs. 8 and 9, the interface positions of the conductivity variation of the homogeneous phantom

are clearly detected and wave packets are generated at the conductivity interfaces, with the amplitude and vibration polarity representing the value and direction of the conductivity variation. Compared with the MAE signals shown in Fig. 8, two narrower MAE wave packets with higher SNR are obtained by our proposed imaging algorithms, and two abrupt conductivity variation interfaces appear in Fig. 9. The above results indicate that the proposed algorithms are effective for improving the imaging resolution of the interface positions of the conductivity variations. The generation mechanism of EMI signal was also confirmed and explained by detecting the locations of the EMI wave packets. As shown in Fig. 10, by applying mean processing, Wiener filtering, Hilbert transform, and interpolation processing, a reconstructed B-scan image with conductivity information is obtained, which is influenced by the noise, partially because of the introduction of the cables for connecting the electrodes. The verification experiment showed that the wrapping copper foil around the wires connecting the electrodes and grounding the copper foil could significantly attenuate the external noise interference. Therefore, further developments are required to formulate more effective approaches and robust algorithms against external noise. In practice, signal averaging and band-pass filtering can be utilized to improve the system SNR in this work.

In addition, according to Eq. (9), the MAE signal only appears at the conductivity variation interfaces, where there are variations in the conductivity gradient. Thus, the relative amplitude of the detected signal was related to the degree of the conductivity variation interface. Therefore, the changes in the conductivity can be characterized by the relative amplitude curve of the MAE signal. After the MAE signal was processed by the imaging algorithms, the relative voltage peaks indicated the conductivity variation interfaces. The interface positions of the conductivity variation and thickness of the phantom measured by our method were consistent with the actual interface positions and mean values obtained by the ultrasound B-mode. This indicated the accuracy and feasibility of the experimental method and detection system. Moreover, the reconstructed B-mode image showed that the proposed MAET detection system could be applied to detect conductivity variation interfaces. The phantom and imaging experiment revealed that conductivity variations occurred only at the boundary regions. However, it was difficult to the distinguish homogeneous regions within the phantom. This problem will be the focus of our future research.

Additionally, the current research studies on MAET detection are in their early stages, the conductivity detection method of MAET and its experimental apparatus need to be improved further. Although some achievements were made, several drawbacks are worth considering and further research is required for optimizing the MAET detection system. These include enhancing the space, field strength, and uniformity of the magnetic field; using a magnetic shielding probe; adopting new techniques and methods to further reduce the EMI signals; improving the platform structure; adding

nanoparticles to the phantom to improve the detection sensitivity; and using a far-field weak focal probe. In this study, a method of separating the EMI signals was proposed and the improved detection system yielded a clear MAE signal and was proved to be effective and accurate for detecting the conductivity variation. However, instead of a complex excitation signal such as a high-excitation voltage signal with a narrow pulse, sinusoid-Barker-coded signal [29], and chirp pulse signal [21], [30] a simple sinusoidal excitation signal was used as the signal source. Therefore, a complex excitation signal and more effective digital signal processing approaches need to be investigated. Moreover, the number of cycles of the sinusoidal excitation signal is one of the main reasons that affect the detection resolution. Therefore, the exploration of the excitation signal is also the focus of our future research. Although the B-mode image was reconstructed using the conductivity interface information, the imaging resolution could be further enhanced. Our experiments were performed only when the transducer moved on the x-axis, and thus, x-axis and y-axis scanning experiments around the target phantom, 3D imaging experiments, and corresponding imaging algorithms are the focus of our future research.

VI. CONCLUSION

In this study, we designed an improved noninvasive MAET detection platform. Both the MAE and EMI signals were measured by our detection platform. The characteristics of the MAE and EMI signals and the influence of the latter on the former were clearly demonstrated. Concurrently, several effective methods for reducing the EMI signal were proposed. A well-separated MAE signal from the EMI signal was obtained clearly, and the imaging algorithms involving mean processing, Wiener filtering, Hilbert transform, and interpolation processing were proposed for obtaining a higher SNR and more accuracy than those achieved without using the algorithms. Finally, a reconstructed B-scan image with the relative amplitude of the conductivity was achieved. The experimental results showed that our MAET detection system could precisely detect the interface positions of the conductivity variation. This demonstrated that the MAET detection system and B-mode imaging algorithm for measuring the interface positions of the conductivity variation were accurate, effective, and feasible. However, in our experiments, only homogeneous phantom experiments were performed for testing; therefore, it is necessary to conduct related experiments on a multilayer phantom with different conductivities and tumor tissues embedded in the homogeneous imitations, which will be the main research content of our next experiments.

REFERENCES

[1] D. Haemmerich, S. T. Staelin, J. Z. Tsai, S. Tungjitkusolmun, D. M. Mahvi, and J. G. Webster, "*In vivo* electrical conductivity of hepatic tumours," *Physiol. Meas.*, vol. 24, no. 2, pp. 251–260, 2003.

[2] C. Gabriel, S. Gabriel, and E. Corthout, "The dielectric properties of biological tissues: I. Literature survey," *Phys. Med. Biol.*, vol. 41, no. 11, pp. 2231–2249, 1996.

[3] W. T. Joines, Y. Zhang, C. Li, and R. L. Jirtle, "The measured electrical properties of normal and malignant human tissues from 50 to 900 MHz," *Med. Phys.*, vol. 21, no. 4, pp. 547–550, 1994.

[4] L. L. Wang, "Early diagnosis of breast cancer," *Sensors*, vol. 17, no. 7, p. 1572, 2017.

[5] Y. Guo, W. Yao, and R. Pei, "Label-free biosensors for early diagnosis of cancer based on G-quadruplex and isothermal amplification," in *Next Generation Point-of-care Biomedical Sensors Technologies for Cancer Diagnosis*. Singapore: Springer, 2017.

[6] P. Metherall, D. C. Barber, R. H. Smallwood, and B. H. Brown, "Three-dimensional electrical impedance tomography," *Nature*, vol. 380, no. 6574, pp. 509–512, 1996.

[7] K. Paulson, W. Lionheart, and M. Pidcock, "Optimal experiments in electrical impedance tomography," *IEEE Trans. Med. Imag.*, vol. 12, no. 4, pp. 681–686, Dec. 1993.

[8] O. F. Oran and Y. Z. Ider, "Magnetic resonance electrical impedance tomography (MREIT) based on the solution of the convection equation using FEM with stabilization," *Phys. Med. Biol.*, vol. 57, no. 16, pp. 5113–5140, 2012.

[9] B. H. Blott, G. J. Daniell, and S. Meeson, "Nonlinear reconstruction constrained by image properties in electrical impedance tomography," *Phys. Med. Biol.*, vol. 43, no. 5, p. 1215, 1998.

[10] B. H. Brown, "Electrical impedance tomography (EIT): A review," *J. Med. Eng. Technol.*, vol. 27, no. 3, pp. 97–108, 2009.

[11] M. Cheney, D. Isaacson, and J. C. Newell, "Electrical impedance tomography," *SIAM Rev.*, vol. 41, no. 1, pp. 85–101, 1999.

[12] D. S. Holder, "Electrical impedance tomography: Methods, history and applications," *Med. Phys.*, vol. 32, no. 8, p. 2731, 2005.

[13] M. Chauhan, W. C. Jeong, H. J. Kim, O. I. Kwon, and E. J. Woo, "Optimization of magnetic flux density for fast MREIT conductivity imaging using multi-echo interleaved partial Fourier acquisitions," *Biomed. Eng. Online*, vol. 12, no. 1, p. 82, 2013.

[14] P. Grasland-Mongrain and C. Lafon, "Review on biomedical techniques for imaging electrical impedance," *IRBM*, vol. 39, pp. 243–250, Aug. 2018.

[15] H. Griffiths, "Magnetic induction tomography," *J. Commun. Technol. Electron.*, vol. 12, no. 8, p. 1126, 2001.

[16] H. Ammari, P. Grasland-Mongrain, P. Millien, L. Seppecher, and J.-K. Seo, "A mathematical and numerical framework for ultrasonically-induced Lorentz force electrical impedance tomography," *J. Math. Pures Appl.*, vol. 103, no. 6, pp. 1390–1409, 2015.

[17] A. Montalibet, J. Jossinet, and A. Matias, "Scanning electric conductivity gradients with ultrasonically-induced Lorentz force," *Ultrason. Imag.*, vol. 23, no. 2, pp. 117–132, 2001.

[18] M. Dai *et al.*, "A 2D magneto-acousto-electrical tomography method to detect conductivity variation using multifocus image method," *Sensors*, vol. 18, no. 7, p. 2373, 2018.

[19] Y. Li, G. Liu, H. Xia, and Z. Xia, "Numerical simulations and experimental study of magneto-acousto-electrical tomography with plane transducer," *IEEE Trans. Magn.*, vol. 54, no. 3, Mar. 2017, Art. no. 5100704.

[20] Y. Xu, S. Haider, and A. Hrbek, "Magneto-acousto-electrical tomography: A new imaging modality for electrical impedance," in *Proc. 13th Int. Conf. Elect. Bioimpedance 8th Conf. Elect. Impedance Tomogr.* Berlin, Germany: Springer Heidelberg, 2007, pp. 292–295.

[21] Z. Sun, G. Liu, L. Guo, H. Xia, and X. Wang, "Effect of the secondary process on mass point vibration velocity propagation in magneto-acoustic tomography and magneto-acousto-electrical tomography," *Technol. Health Care Off. J. Eur. Soc. Eng. Med.*, vol. 24, no. s2, pp. S683–S689, 2016.

[22] M. Dai, X. Chen, M. Chen, H. Lin, F. Li, and S. Chen, "A novel method to detect interface of conductivity changes in magneto-acousto-electrical tomography using chirp signal excitation method," *IEEE Access*, vol. 6, pp. 33503–33512, 2018.

[23] A. S. Rekhi and A. Arbabian, "Remote sub-wavelength focusing of ultrasonically activated lorentz current," *Appl. Phys. Lett.*, vol. 110, no. 16, 2017, Art. no. 164104.

[24] H. Wen, J. Shah, and R. S. Balaban, "Hall effect imaging," *IEEE Trans. Biomed. Eng.*, vol. 45, no. 1, pp. 119–124, Jan. 1998.

[25] S. Haider, A. Hrbek, and Y. Xu, "Magneto-acousto-electrical tomography: A potential method for imaging current density and electrical impedance," *Physiol. Meas.*, vol. 29, no. 6, pp. S41, 2008.

[26] B. J. Roth and K. Schalte, "Ultrasonically-induced Lorentz force tomography," *Med. Biol. Eng. Comput.*, vol. 47, no. 6, pp. 573–577, 2009.

[27] L. Kunyansky, "A mathematical model and inversion procedure for magneto-acousto-electric tomography," *Inverse Problems*, vol. 28, no. 3, pp. 35002–35022, 2011.

[28] Y. Xu, and B. He, "Magnetoacoustic tomography with magnetic induction (MAT-MI)," *IEEE Trans. Med. Imag.*, vol. 29, no. 10, pp. 1759–1767, 2010.

[29] Z. F. Yu *et al.*, "Performance improvement of magneto-acousto-electrical tomography for biological tissues with sinusoid-Barker coded excitation," *Chin. Phys. B*, vol. 27, no. 9, pp. 0943021–0943028, 2018.
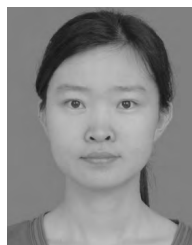
[30] Z. Sun, G. Liu, H. Xia, and S. Catheline, "Lorentz force electrical-impedance tomography using linearly frequency-modulated ultrasound pulse," *IEEE Trans. Ultrason., Ferroelectr., Freq. Control*, vol. 65, no. 2, pp. 168–177, Feb. 2018.

[31] P. Grasland-Mongrain, F. Destrempes, J. M. Mari, and R. Souchon, "Acousto-electrical speckle pattern in Electrical Impedance Tomography," *Inst. Phys. Eng. Med.*, vol. 60, no. 9, pp. 3747–3757, 2015.

[32] Y. Zhou, Q. Ma, G. Guo, J. Tu, and D. Zhang, "Magneto-acousto-electrical measurement based electrical conductivity reconstruction for tissues," *IEEE Trans. Biomed. Eng.*, vol. 65, no. 5, pp. 1086–1094, May 2017.

[33] H. Xia, G. Liu, and X. Zeng, "Experimental study of magneto-acousto-electrical tomography," in *Proc. IEEE 2nd Int. Conf. Mech. Automat. Control Eng.*, Jul. 2011, pp. 1310–1313.

[34] A. Salari, M. Navi, and C. Dalton, "A novel alternating current multiple array electrothermal micropump for lab-on-a-chip applications," *Biomicrofluidics*, vol. 9, no. 1, 2015, Art. no. 014113.

MING DAI received the B.S. degree in computer science and technology from Hainan Tropical Ocean University, Sanya, Hainan, in 2012, and the M.S. degree in electronics and communication engineering from Nanchang Hangkong University, Nanchang, Jiangxi, and the Shenzhen Institutes of Advanced Technology, Chinese Academy of Sciences, Shenzhen, Guangdong, in 2015. He is currently pursuing the Ph.D. degree with Shenzhen University for learning and scientific research. His research interests include electrical conductivity imaging, biomedical multimodal data fusion, image processing, wearable medical applications, and design of electrical systems.

TONG SUN received the B.S. degree in biomedical engineering from Northeastern University, China, in 2016. He is currently pursuing the M.S. degree in biomedical engineering with Shenzhen University, Shenzhen, China. His research interests include medical ultrasonic imaging and biomedical conductivity imaging.

XIN CHEN received the B.S. degree in electrical engineering and the Ph.D. degree in biomedical engineering from the University of Science and Technology of China, in 1998 and 2003, respectively. He then joined the Department of Health Technology and Informatics, The Hong Kong Polytechnic University, as a Research Associate. In 2008, he joined the Department of Biomedical Engineering, Shenzhen University, as an Assistant Professor and became an Associate Professor, in 2011, and a Professor, in 2017. His research interests include ultrasound elasticity imaging and measurement, ultrasound assessment of musculoskeletal tissues, biomedical conductivity imaging, and biomedical instrumentation.

LINGYAO YU received the B.S. degree in optical information science and technology from Jiangnan University, in 2007, the M.S. degree in physical electronics from Shenzhen University, China, in 2010, and the Ph.D. degree in physics from Laval University, Quebec, Canada, in 2016. She completed her Postdoctoral Research in COPL, Laval University, in 2017. She is currently an Associate Professor with the Guilin University of Electronic Technology, Guilin, China. Her research interests include finite-element analysis, electromagnetics, ultrasound, optics, solid mechanics, and biophotonics.

MIAN CHEN received the Ph.D. degree in analytical chemistry from Hunan University, China, in 2014. He is currently an Associate Researcher with the School of Biomedical Engineering, Shenzhen University. His research interests include using functional nanomaterials for cancer diagnosis and treatment.

PENGHUI HAO received the B.S. degree in biomedical engineering from Zhengzhou University, China, in 2017. He is currently pursuing the M.S. degree in biomedical engineering with Shenzhen University, Shenzhen, China. His research interests include medical ultrasonic imaging and biomedical conductivity imaging.

XIN ZENG received the B.S. degree in biomedical engineering from Southern Medical University, China, in 2016. He is currently pursuing the M.S. degree in biomedical engineering with Shenzhen University, Shenzhen, China. His research interests include medical ultrasonic imaging and biomedical conductivity imaging.
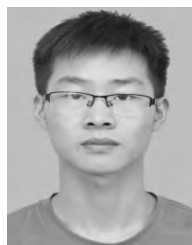
JIEJIE YAN received the B.S. degree in biomedical engineering from Nanchang Hangkong University, China, in 2017. He is currently pursuing the M.S. degree in biomedical engineering with Shenzhen University, Shenzhen, China. His research interest includes *ex vivo* dielectric property measurements of tissues based on bioimpedance methods.

SIPING CHEN received the Ph.D. degree in biomedical engineering from Xi'an Jiaotong University, Shanxi, China, in 1987. After a Postdoctoral Fellowship at Zhejiang University, Zhejiang, China, he joined Shenzhen Anke High-tech Co., Ltd., as a Chief Technology Officer, in 1989. Having served at Shenzhen Anke High-tech Co., Ltd., for 16 years, he joined Shenzhen University, as a Vice President, and founded the Biomedical Engineering Branch, in 2005. His main research interests include biomedical ultrasound imaging, medical instrumentation, tissue elasticity imaging, multimodal ultrasound imaging, and image processing.

• • •